Academic Journal of Science and Technology
ISSN: 2771-3032 | Vol. 10, No. 1, 2024

Enhanced Thermoelectric Performance in Ca-doped $AgSbTe_2$

Yi Pan*

School of Physics and Optoelectronic Engineering, Guangdong University of Technology, Guangzhou, 510006, China
* Corresponding author

Abstract: Thermoelectric materials play a crucial role in applications such as recovering waste heat and refrigeration. We report a thermoelectric figure of merit (zT) of 1.17 at 623 K for $AgSb_{1-x}Ca_xTe_2$, representing a 31% enhancement compared to pristine $AgSbTe_2$. The improved thermoelectric performance arises from enhancements in both the power factor and lattice thermal conductivity. Dopant substitution of element Ca at the Sb site in $AgSbTe_2$ suppresses the formation of Ag_2Te and increases the concentration of p-type charge carriers, leading to enhanced electrical transport properties. Additionally, Ca doping introduces solid solution point defects that enhance phonon scattering, consequently reducing the lattice thermal conductivity of the sample. This work demonstrates that a doping effectively modulates the electrical and thermal transport properties of $AgSbTe_2$, thereby realizing improvements in thermoelectric performance.

1. Introduction

As the demand for energy in human society continues to increase, the issue of energy recycling is gradually gaining attention. Thermoelectric (TE) materials, due to their ability to achieve direct reversible conversion between heat and electricity, have been continuously attracting attention in recent years[1-3]. The performance of TE materials is described by the dimensionless thermoelectric figure of merit, $zT=\sigma S^2T/\kappa$, where σ, S, T, and κ represent the electrical conductivity, Seebeck coefficient, absolute temperature, and thermal conductivity, respectively[4]. High-performance TE materials require properties resembling those of metals for σ, large values for S, and low values for κ. However, these parameters are mutually restrictive, making the enhancement of TE performance challenging[5].

Currently, researchers have developed various strategies to optimize the TE performance of materials. To achieve a high power factor (σS^2), precise control over the carrier concentration of the material is necessary[4]. Aliovalent doping, which introduces additional electrons or holes, is an effective method for controlling carrier concentration[2, 3, 6]. Band engineering, such as band convergence[7-10], band flattening[11-13], and resonant energy levels[3, 14], can enhance the electrical transport properties of materials without increasing κ. Thermal conductivity (κ) comprises electronic thermal conductivity (κ_{ele}) and lattice thermal conductivity (κ_{lat}). κ_{ele} is related to electrical conductivity and is difficult to adjust independently. However, κ_{lat} can be independently optimized through methods such as doping[15-18], composite multiphase nanostructure[2, 19-21], and ball milling[22-25]. Furthermore, exploring new materials with inherently low thermal conductivity is also an important aspect of research in the field of TE materials[1, 26-29].

$AgSbTe_2$ exhibits intrinsically low κ_{lat} due to strong bond anharmonicity arising from the $5s^2$ lone pair electrons in Sb[30] and spontaneously formed nano-scale superstructures[31, 32]. However, its relatively lower σS^2 do not make its zT value outstanding among mid-temperature TE materials. Many groups have made remarkable efforts to improve the TE performance of $AgSbTe_2$. Roychowdhury et al.[33] increased the σ of $AgSbTe_2$ at 300K from ~136 S cm^{-1} to 160 S cm^{-1} by doping Zn into the Sb site. Wang et al.[24] introduced dense interfaces in $AgSbTe_2$ through ball milling and SPS techniques, leading to a significant reduction in κ of the material. Du et al.[34] enhanced the electrical transport properties of $AgSbTe_2$ by suppressing the formation of Ag_2Te impurity phases through Mg doping. The relatively low σS^2 of $AgSbTe_2$ stems from its lower carrier concentration. As Ca has one fewer valence electron than Sb, it is expected that by doping Ca, additional holes can be introduced to increase the p-type carrier concentration of the material, thereby enhancing the TE performance of $AgSbTe_2$.

In this work, we prepared polycrystalline samples of $AgSb_{1-x}Ca_xTe_2$ (x=0, 0.01, 0.02, 0.03, 0.04) using a melt-quench-anneal method. The results indicate that for samples with $x\leq0.03$, Ca doping suppresses the formation of Ag_2Te impurity phases and increases the p-type carrier concentration, leading to an enhancement in σ. However, as the Ca content further increases, impurity phases such as CaTe and Ag_7Te_4 begin to appear, adversely affecting the electrical transport properties of the samples. Due to the introduction of point defect structures, the κ_{lat} of all Ca-doped samples is reduced. However, due to the increased κ_{ele}, the κ of Ca-doped samples is slightly higher than that of pristine $AgSbTe_2$. Ultimately, owing to the significant improvement in σS^2, the $AgSb_{0.97}Ca_{0.03}Te_2$ sample achieves a maximum zT value of ~1.17 at 623 K, representing a 31% enhancement compared to pristine $AgSbTe_2$.

2. Experiment

According to the proportions of $AgSb_{1-x}Ca_xTe_2$ (x=0, 0.01, 0.02, 0.03, 0.04), high-purity silver (Aladdin 99.95%), antimony (Aladdin 99.999%), calcium (Aladdin 99.95%), and tellurium (Aladdin 99.99%) elements were weighed. The raw materials were mixed and thoroughly ground in an argon atmosphere glovebox, and then the mixed powder was sealed in a vacuum quartz tube. The quartz tube was heated to 723 K within 12 hours and held for 3 hours, then heated to 1223 K within 3 hours and held for 15 hours, followed by quenching in water. Finally, the samples were annealed at 923 K for 3 days.

The X-ray diffraction (XRD) of the samples was recorded using Cu Kα (λ=1.5406 Å) radiation on a Rigaku Ultima-IV diffractometer. The microstructure of the samples was investigated using scanning electron microscopy (SEM, Thermo Fisher Scientific, Apreo 2S HiVac), and the composition and elemental distribution of the samples were analyzed using backscattered electron imaging (BSE) and energy-dispersive X-ray spectroscopy (EDS). The σ and S of the samples were simultaneously measured between 300 - 600 K using the JouleYacht Namicro-III thermoelectric parameter testing system, with a measurement uncertainty of 5%. The Hall coefficient (R_H) of the samples was measured at room temperature using a Nanometrics HL5500 Hall effect tester with a magnetic field intensity of ±0.5 T. The Hall carrier concentration (n_H) and Hall carrier mobility (μ_H) were calculated using $n_H = 1/eR_H$ and $\mu_H = \sigma|R_H|$, respectively. The thermal diffusivity (D) of the samples was measured using laser flash analysis on a Netzsch LFA-467, with an uncertainty of 3%. The thermal conductivity (κ) was calculated using $\kappa = D\rho C_p$, where ρ and C_p are the density and specific heat capacity, respectively. The ρ was determined using the Archimedes method, and the C_p was determined using the Dulong-Petit law[35]. The κ_{ele} was calculated using $\kappa_{ele}=L\sigma T$, where L is the Lorenz number, calculated according to the formula proposed by G. J. Snyder et al.[36], $L = [1.5 + \exp(-|S|/116)]\ 10^{-8}\ W\Omega K^{-2}$. The κ_{lat} was calculated as $\kappa_{lat} = \kappa - \kappa_{ele}$.

3. Results and Discussion

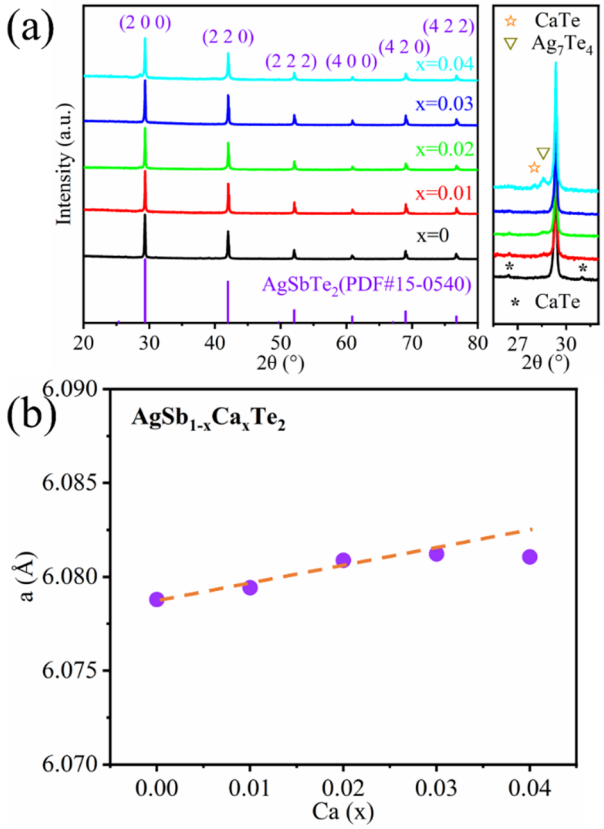

Figure 1. (a) XRD patterns of $AgSb_{1-x}Ca_xTe_2$ (x=0, 0.01, 0.02, 0.03, 0.04) samples (left); enlarged XRD patterns near the (200) diffraction peak (right). (b) Variation of lattice parameter as a function of Ca (x) content in $AgSb_{1-x}Ca_xTe_2$.

Figure 1(a) shows the XRD patterns of $AgSb_{1-x}Ca_xTe_2$ samples. The diffraction peaks of all samples correspond to the standard card (PDF#15-0540), indexing to the face-centered cubic $AgSbTe_2$ with the space group Fm-3m[37-39]. In the enlarged panel on the right near the (200) diffraction peak, it can be observed that there is a small amount of Ag_2Te impurity phase (PDF#34-0142) present in pristine $AgSbTe_2$. With the increase in Ca doping, the amount of Ag_2Te impurity phase gradually decreases. In the XRD patterns of x=0.03 and x=0.04, the Ag_2Te impurity phase almost disappears, indicating that Ca doping helps to reduce the formation of Ag_2Te. Meanwhile, in the x=0.04 Ca-doped sample, small amounts of CaTe and Ag_7Te_4 impurity phases were detected. Figure 1(b) shows the lattice parameters of $AgSb_{1-x}Ca_xTe_2$ samples calculated from the XRD data. The lattice parameter of pristine $AgSbTe_2$ is approximately 6.079 Å, consistent with reported literature data[10, 33]. With the increase in Ca content, the lattice parameters of $AgSb_{1-x}Ca_xTe_2$ gradually increase. This is because the radius of Ca^{2+} (100 Å) is larger than that of Sb^{3+} (76 Å), leading to lattice expansion due to Ca doping. For the sample with x=0.04, the lattice parameter no longer increase, which corresponds to the appearance of CaTe precipitation, indicating that the doping level of x=0.04 has exceeded the solubility limit of Ca in $AgSbTe_2$.

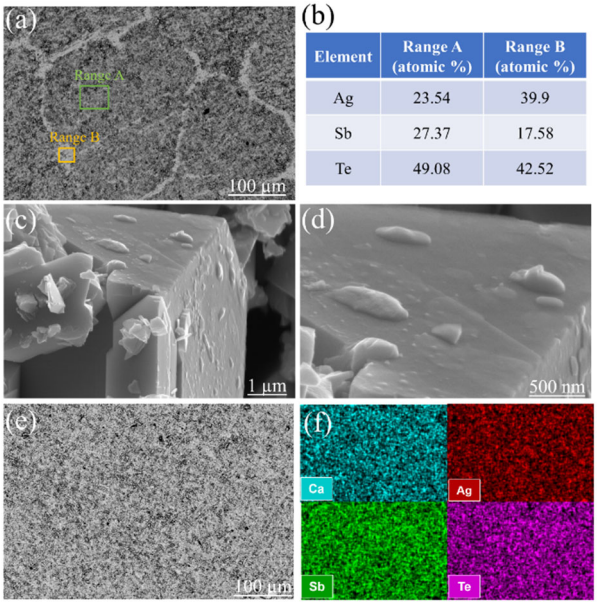

Element	Range A (atomic %)	Range B (atomic %)
Ag	23.54	39.9
Sb	27.37	17.58
Te	49.08	42.52

Figure 2. (a) BSE image, (b) EDS results within ranges A and B, and (c, d) SEM images of $AgSbTe_2$. (e) BSE image and (f) EDS mapping of $AgSb_{0.97}Ca_{0.03}Te_2$.

To understand the surface morphology and composition of $AgSb_{1-x}Ca_xTe_2$ samples, BSE imaging and EDS element analysis were performed. Figure 2(a) shows the BSE image of pristine $AgSbTe_2$, where distinct contrast differences are observed on the sample surface, indicating significant variations in elemental composition among different regions. Therefore, EDS analysis was conducted on ranges A and B, and the results are shown in Figure 2(b). It can be observed that there is a slight deficiency of Ag element in range A compared to the nominal content. Conversely, the Ag content in range B is much higher than the nominal content, while the Sb content is relatively lower. Combined with the observation of Ag_2Te impurity phase in the XRD data of $AgSbTe_2$, the abnormal variation in element content in range B is attributed to the enrichment of Ag_2Te precipitation. Subsequently, we observed the cross-section of the $AgSbTe_2$ sample at higher magnifications using SEM. As shown in Figures 2(c, d),

numerous nanoscale precipitates, corresponding to Ag_2Te precipitation, are present on the surface of the pristine $AgSbTe_2$ sample. During the cooling process of the $AgSbTe_2$ melt, Ag_2Te nucleates and grows into nanoscale precipitates in the matrix due to its higher melting point, leading to a deficiency of Ag in the $AgSbTe_2$ matrix and enrichment of Ag at grain boundaries. For the x=0.03 Ca-doped sample, no significant contrast differences were observed in the BSE image (Figure 2(e)). The EDS mapping showed uniform elemental distribution without any signs of elemental enrichment, indicating that Ca doping suppressed the formation of Ag_2Te precipitation (Figure 2(f)). For the p-type semiconductor $AgSbTe_2$, the presence of Ag_2Te precipitation not only reduces the hole concentration but also deteriorates the carrier mobility. Through Ca doping, the formation of Ag_2Te precipitation is significantly suppressed[34]. Therefore, the electrical transport properties of the $AgSb_{1-x}Ca_xTe_2$ sample are improved, which will be discussed in detail in the following sections.

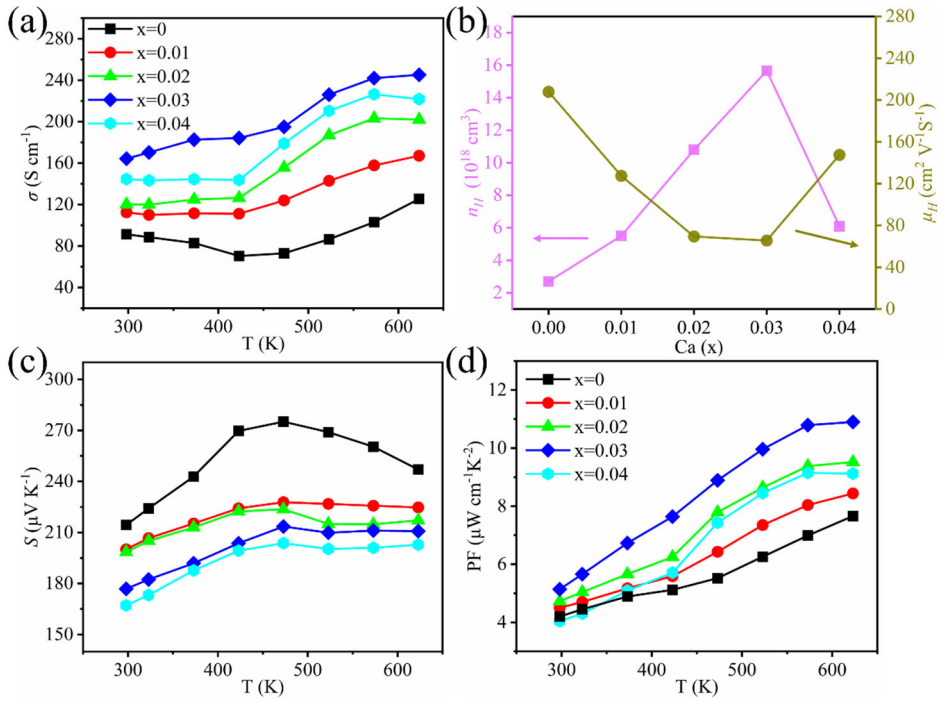

Figure 3. Temperature-dependent (a) electrical conductivity, (b) variation of room-temperature carrier concentration and mobility as a function of Ca (x) content, (c) Seebeck coefficient, and (d) power factor for $AgSb_{1-x}Ca_xTe_2$ (x=0, 0.01, 0.02, 0.03, 0.04) samples.

Figure 3(a) shows the temperature-dependent of the σ for $AgSb_{1-x}Ca_xTe_2$ samples. The σ of pristine $AgSbTe_2$ at 300 K is 91 S cm^{-1}. As the temperature increases, the σ of $AgSbTe_2$ first decreases and then increases, exhibiting characteristics of a degenerate semiconductor. With increasing Ca content, the σ of AgSb1-xCaxTe2 samples gradually increases. For the $AgSb_{0.97}Ca_{0.03}Te_2$ sample, the σ at 300 K increases to 164 S cm^{-1}. To understand the reason for the increase in σ for Ca-doped samples, Hall tests were conducted to estimate the n_H and μ_H of $AgSb_{1-x}Ca_xTe_2$ samples, as shown in Figure 3(b). With increasing Ca doping, the p-type carrier concentration of the sample gradually increases from 2.7×10^{18} cm^{-1} for pristine $AgSbTe_2$ to 14.2×10^{18} cm^{-1} for $AgSb_{0.97}Ca_{0.03}Te_2$. This indicates that Ca^{2+} is doped into the Sb^{3+} lattice sites, providing one hole per doping site for $AgSb_{1-x}Ca_xTe_2$. Due to the enhancement of carrier scattering and ionized impurity scattering, the μ_H of Ca-doped samples decreases. However, due to the suppression of Ag_2Te impurity phase, the μ_H of the $AgSb_{0.97}Ca_{0.03}Te_2$ sample hardly decreases compared to $AgSb_{0.98}Ca_{0.02}Te_2$, resulting in an enhancement of σ. When the Ca content increases to x=0.04, the σ of the sample begins to decrease. As shown in Figure 3(b), the n_H of $AgSb_{0.96}Ca_{0.04}Te_2$ is significantly lower compared to $AgSb_{0.97}Ca_{0.03}Te_2$. This is mainly attributed to two reasons: (1) According to the XRD data, the Ca doping level at x=0.04 has exceeded the solubility limit, and the excess Ca no longer provides holes for the system. (2) The formation of Ag_7Te_4 impurity phase provides free electrons to the system, leading to a decrease in p-type carrier concentration. This phenomenon is represented by the defect reaction equation:

$$AgSb_{0.97}Ca_{0.04}Te_2 \rightarrow xAg_7Te_4 + Ag_{1-7x}Sb_{0.97}Ca_{0.04}Te_{2-4x} + 7xV'_{Ag} + 4xV^{\bullet\bullet}_{Te} + xe' \quad (1)$$

For a degenerate semiconductor with parabolic band dispersion, the S is given by the following equation:

$$S = \frac{8\pi^2 k_B^2}{3eh^2} m^* T \left(\frac{\pi}{3n}\right)^{2/3} \quad (2)$$

where k_B is the Boltzmann constant, e is the elementary charge, h is the Planck constant, m^* is the effective mass of carriers, and n is the carrier concentration. The S is inversely proportional to the n. Due to the increase in n resulting from Ca doping, the S of $AgSb_{1-x}Ca_xTe_2$ samples is lower than that of pristine $AgSbTe_2$. However, the increase in σ compensates for the decrease in S, resulting in an enhancement of the power factor for $AgSb_{0.97}Ca_{0.03}Te_2$, reaching a maximum value of 10.79 μW $cm^{-1}K^{-2}$ at 623 K.

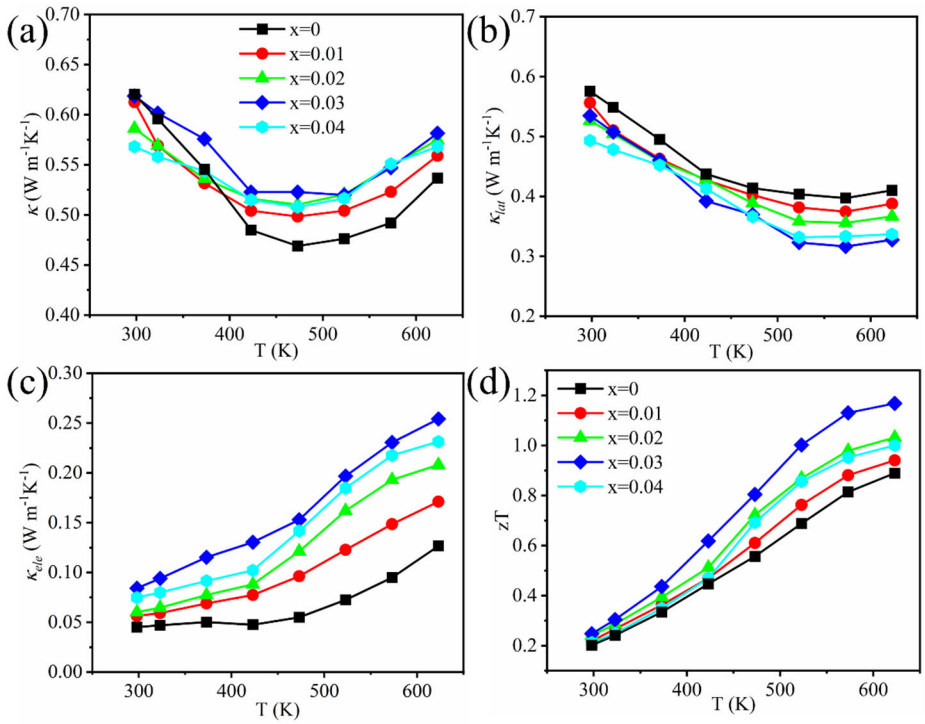

Figure 4. Temperature-dependent (a) thermal conductivity, (b) electronic thermal conductivity, (c) lattice thermal conductivity, and (d) zT values for $AgSb_{1-x}Ca_xTe_2$ (x=0, 0.01, 0.02, 0.03, 0.04) samples.

Figure 4 (a) shows the temperature-dependent κ of $AgSb_{1-x}Ca_xTe_2$ samples. At 300 K, the κ of pristine $AgSbTe_2$ is 0.62 W $m^{-1}K^{-1}$. With increasing temperature, the κ of $AgSbTe_2$ gradually decreases, reaching a minimum of 0.47 W $m^{-1}K^{-1}$ at 473 K. Beyond 473 K, due to the onset of bipolar conduction, the κ of $AgSbTe_2$ starts to increase. At 300 K, the κ of the Ca-doped samples is lower than that of pristine $AgSbTe_2$. To understand this phenomenon, the κ_{lat} and κ_{ele} of $AgSb_{1-x}Ca_xTe_2$ samples are calculated, as shown in Figures 4(b) and 4(c), respectively. From Figure 4(b), it can be observed that the κ_{lat} of all Ca-doped samples is lower than that of pristine $AgSbTe_2$, attributed to the introduction of point defects by Ca doping, enhancing phonon scattering in the samples. Although the κ_{ele} of the Ca-doped samples increases at 300 K, the decrease in κ_{lat} is more significant, leading to a reduction in κ. However, with increasing temperature, the κ of the Ca-doped samples starts to exceed that of pristine $AgSbTe_2$ samples. As shown in Figure 4(c), this is primarily due to a significant increase in the κ_{ele} of the Ca-doped samples at high temperatures. For example, the κ_{ele} of $AgSb_{0.97}Ca_{0.03}Te_2$ increases by 0.17 W $m^{-1}K^{-1}$ at 623 K compared to that at 300 K, whereas in pristine $AgSbTe_2$, this value is only 0.08 W $m^{-1}K^{-1}$. This phenomenon may be attributed to the lower electronegativity of Ca compared to Sb, resulting in a reduced bandgap due to Ca doping, thereby exciting more electrons at high temperatures. Ultimately, due to the enhancement in power factor and reduction in κ_{lat}, the thermoelectric performance of $AgSb_{0.97}Ca_{0.03}Te_2$ is improved, achieving a maximum zT value of ~1.17 at 623 K, representing a 31% enhancement compared to pristine $AgSbTe_2$.

4. Conclusion

In this work, we achieved a maximum zT value of ~1.17 in $AgSb_{1-x}Ca_xTe_2$ by partially substituting Sb with Ca, representing a 31% enhancement compared to pristine $AgSbTe_2$. The improved thermoelectric performance stems from the enhancement in power factor and the reduction in lattice thermal conductivity. The increase in power factor is attributed to the suppression of Ag_2Te impurity phase and the increase in p-type carrier concentration due to Ca doping, resulting in a significant enhancement in electrical conductivity while maintaining a high Seebeck coefficient. Meanwhile, the reduction in lattice thermal conductivity is attributed to the introduction of substitutional defects, which enhances phonon scattering in the material. This work confirms that Ca doping can improve the electrical and thermal transport properties of $AgSbTe_2$, achieving enhanced thermoelectric performance.

References

[1] A. Bhui, M. Dutta, M. Mukherjee, K. S. Rana, A. K. Singh, A. Soni, K. Biswas. Chemistry of Materials. 33, 8 (2021).

[2] K. Biswas, J. He, I. D. Blum, C.-I. Wu, T. P. Hogan, D. N. Seidman, V. P. Dravid, M. G. Kanatzidis. Nature. 489, 7416 (2012).

[3] Y.-P. Wang, B.-C. Qin, D.-Y. Wang, T. Hong, X. Gao, L.-D. Zhao. Rare Metals. 40, 10 (2021).

[4] G. Tan, L.-D. Zhao, M. G. Kanatzidis. Chemical Reviews. 116, 19 (2016).

[5] X. Zhou, Y. Yan, X. Lu, H. Zhu, X. Han, G. Chen, Z. Ren. Materials Today. 21, 9 (2018).

[6] M. Li, Y. Zhang, T. Zhang, Y. Zuo, K. Xiao, J. Arbiol, J. Llorca, Y. Liu, A. Cabot. Nanomaterials. 11, 7 (2021).

[7] Y. Pei, X. Shi, A. LaLonde, H. Wang, L. Chen, G. J. Snyder. Nature. 473, 7345 (2011).

[8] H. Wu, C. Chang, D. Feng, Y. Xiao, X. Zhang, Y. Pei, L. Zheng, D. Wu, S. Gong, Y. Chen, J. He, M. G. Kanatzidis, L.-D. Zhao. Energy & Environmental Science. 8, 11 (2015).

[9] L. D. Zhao, H. J. Wu, S. Q. Hao, C. I. Wu, X. Y. Zhou, K. Biswas, J. Q. He, T. P. Hogan, C. Uher, C. Wolverton, V. P.

Dravid, M. G. Kanatzidis. Energy & Environmental Science. 6, 11 (2013).

[10] M. Hong, Z.-G. Chen, L. Yang, Z.-M. Liao, Y.-C. Zou, Y.-H. Chen, S. Matsumura, J. Zou. Advanced Energy Materials. 8, 9 (2018).

[11] Y. Xiao, H. Wu, J. Cui, D. Wang, L. Fu, Y. Zhang, Y. Chen, J. He, S. J. Pennycook, L.-D. Zhao. Energy & Environmental Science. 11, 9 (2018).

[12] X. Qian, H. Wu, D. Wang, Y. Zhang, J. Wang, G. Wang, L. Zheng, S. J. Pennycook, L.-D. Zhao. Energy & Environmental Science. 12, 6 (2019).

[13] Y. Zhang, Z. Li, S. Singh, A. Nozariasbmarz, W. Li, A. Genc, Y. Xia, L. Zheng, S. H. Lee, S. K. Karan, G. K. Goyal, N. Liu, S. M. F. Mohan, Z. Mao, A. Cabot, C. Wolverton, B. Poudel, S. Priya. Advanced Materials. (2023).

[14] C. M. Jaworski, V. Kulbachinskii, J. P. Heremans. Physical Review B. 80, 23 (2009).

[15] T. Zhu, L. Hu, X. Zhao, J. He. Advanced Science. 3, 7 (2016).

[16] K. Li, Z. Li, L. Yang, C. Xiao, Y. Xie. Inorganic Chemistry. 58, 14 (2019).

[17] B.-K. Min, B.-S. Kim, M.-W. Oh, B.-K. Ryu, J.-E. Lee, S.-J. Joo, S.-D. Park, H.-W. Lee, H.-s. Lee. Journal of the Korean Physical Society. 68, 1 (2016).

[18] R. Mohanraman, R. Sankar, F. C. Chou, C. H. Lee, Y.-Y. Chen. Journal of Applied Physics. 114, 16 (2013).

[19] J. Zhang, D. Wu, D. He, D. Feng, M. Yin, X. Qin, J. He. Advanced Materials. 29, 39 (2017).

[20] R. Mohanraman, R. Sankar, F.-C. Chou, C.-H. Lee, Y. Iizuka, I. P. Muthuselvam, Y.-Y. Chen. Apl Materials. 2, 9 (2014).

[21] B. Cai, J. Pei, J. Dong, H.-L. Zhuang, J. Gu, Q. Cao, H. Hu, Z. Lin, J.-F. Li. Science China-Materials. 64, 10 (2021).

[22] W. Lu, X. Lai, Q. Liu, Z. He, H. Zhao, J. Jian. Ceramics International. 47, 18 (2021).

[23] B. Du, H. Li, J. Xu, X. Tang, C. Uher. Journal of Solid State Chemistry. 184, 1 (2011).

[24] H. Wang, J.-F. Li, M. Zou, T. Sui. Applied Physics Letters. 93, 20 (2008).

[25] Y. Wu, Q. Liang, X. Zhao, H. Wu, P. Zi, Q. Tao, L. Yu, X. Su, J. Wu, Z. Chen, Q. Zhang, X. Tang. Acs Applied Materials & Interfaces. 14, 2 (2022).

[26] M. Samanta, K. Biswas. Chemistry of Materials. 32, 20 (2020).

[27] M. Samanta, K. Pal, P. Pal, U. V. Waghmare, K. Biswas. Journal of the American Chemical Society. 140, 17 (2018).

[28] J. Ma, O. Delaire, A. F. May, C. E. Carlton, M. A. McGuire, L. H. VanBebber, D. L. Abernathy, G. Ehlers, T. Hong, A. Huq, W. Tian, V. M. Keppens, Y. Shao-Horn, B. C. Sales. Nature Nanotechnology. 8, 6 (2013).

[29] D. T. Morelli, V. Jovovic, J. P. Heremans. Physical Review Letters. 101, 3 (2008).

[30] M. D. Nielsen, V. Ozolins, J. P. Heremans. Energy & Environmental Science. 6, 2 (2013).

[31] S. Roychowdhury, T. Ghosh, R. Arora, M. Samanta, L. Xie, N. K. Singh, A. Soni, J. He, U. V. Waghmare, K. Biswas. Science. 371, 6530 (2021).

[32] T. Ghosh, S. Roychowdhury, M. Dutta, K. Biswas. Acs Energy Letters. 6, 8 (2021).

[33] S. Roychowdhury, R. Panigrahi, S. Perumal, K. Biswas. Acs Energy Letters. 2, 2 (2017).

[34] R. Du, G. Zhang, M. Hao, X. Xuan, P. Peng, P. Fan, H. Si, G. Yang, C. Wang. Acs Applied Materials & Interfaces. 15, 7 (2023).

[35] H. J. Wu, T. W. Lan, S. W. Chen, Y. Y. Chen, T. Day, G. J. Snyder. Acta Materialia. 93, (2015).

[36] H.-S. Kim, Z. M. Gibbs, Y. Tang, H. Wang, G. J. Snyder. Apl Materials. 3, 4 (2015).

[37] R. W. Armstrong, J. W. Faust, Jr., W. A. Tiller. Journal of Applied Physics. 31, 11 (2004).

[38] S. N. Zhang, T. J. Zhu, S. H. Yang, C. Yu, X. B. Zhao. Journal of Alloys and Compounds. 499, 2 (2010).

[39] R. Pathak, L. Xie, S. Das, T. Ghosh, A. Bhui, K. Dolui, D. Sanyal, J. He, K. Biswas. Energy & Environmental Science. 16, 7 (2023).